

# Nanoscale mapping of internal magnetization dynamics reveals how disorder shapes heat generation in magnetic particle hyperthermia

Elizabeth M. Jefremovas,<sup>1,2,\*</sup> Pauline Rooms,<sup>3</sup> Álvaro Gallo-Córdova,<sup>4</sup> María P. Morales,<sup>4</sup> Frank Wiekhorst,<sup>5</sup> Andreas Michels,<sup>1</sup> and Jonathan Leliaert<sup>3</sup>

<sup>1</sup>*Department of Physics and Materials Science, University of Luxembourg, 162A Avenue de la Faiencerie, L-1511 Luxembourg, Grand Duchy of Luxembourg*

<sup>2</sup>*Institute for Advanced Studies, University of Luxembourg, Campus Belval, L-4365 Esch-sur-Alzette, Luxembourg*

<sup>3</sup>*DyNaMat, Department of Solid State Sciences, Ghent University, 9000 Ghent, Belgium*

<sup>4</sup>*Instituto de Ciencia de Materiales de Madrid (ICMM-CSIC), Madrid 28049, Spain*

<sup>5</sup>*Physikalisch-Technische Bundesanstalt, D-10587 Berlin, Germany*

(Dated: March 17, 2026)

Magnetic particle hyperthermia relies on the efficient conversion of magnetic field energy into heat in biomedical applications, yet the microscopic mechanisms governing heat generation within individual particles remain poorly understood. In this study, AC magnetometry experiments are combined with dynamic micromagnetic simulations to connect microstructural features, magnetization dynamics, and macroscopic heat dissipation. Beyond macroscopic heating metrics, the heat generation is resolved at the intra-particle level, uncovering a heterogeneous landscape of localized “hot spots” with nanometer spatial and nanosecond temporal resolution. The results demonstrate that grain size acts as a key experimentally tunable parameter, balancing anisotropy disorder and pinning strength, thereby controlling both the magnitude and spatio-temporal distribution of heat release within the particle. In particular, nanoflower architectures composed by larger grains deliver larger heat generation, while the smaller grains offer a deeper intra-particle pinning landscape, which effectively redistributes the heat generation over extended time windows. Together, our results provide a mechanistic framework linking nanoparticle microstructure to magnetic heating and establish design principles for optimizing nanoflowers as magnetic hyperthermia transducers.

## INTRODUCTION

Iron oxide nanoparticles (IONPs) represent a class of materials with excellent magnetic properties and with suitable biocompatibility for clinical use [1–4]. One of the distinctive properties of IONPs is their capability to generate heat under the application of an alternating (AC) magnetic field. Acting as nanotransducers converting magnetic field energy into heat, this capability of the IONPs is primarily leveraged in magnetic hyperthermia therapy (MHT) to disrupt the activity of cancerous cells [5, 6]. In recent years, its scope has been expanded to integrate the heat in magnetic particle imaging [7], neuromodulation [8], drug delivery applications [9], as well as emerging fields such as catalysis and environmental remediation [8, 10].

The heating capability of IONPs has been extensively demonstrated experimentally [5, 11–13]. This includes early evidence of heat generation at subnanometer distances from the particle surface [14], and cellular studies showing that magnetic hyperthermia-induced damage is not associated with a global temperature rise but rather with localized, single-cell mechanisms [15]. However, the microscopic origin of this heat generation remains largely unexplored. In particular, little is known

about how heat is produced and distributed within individual nanoparticles, especially beyond the single-domain limit, where spin textures directly affecting the macroscopic magnetic properties emerge [16–18] and magnetic disorder becomes prominent [19]. Elucidating the spatial and temporal intra-particle heat landscape, *i.e.*, the nanoscale distribution of “hot spots”, and linking it to structural and magnetic inhomogeneities is therefore essential to rationally tailor heat generation and enable optimized nanoparticle design for magnetic hyperthermia. This is particularly relevant in multi-core ensembles, where their multi-grain structure affect markedly their macroscopic magnetic properties even within the nominal single-domain regime [12, 20].

Using a micromagnetic framework, we describe the magnetization dynamics of multicore iron-oxide nanoparticles, referred to as nanoflowers (NFs) (see Figure 1), whose magnetization folds into a vortex for sizes  $d > 70$  nm. Such a spin texture is highly relevant for biomedical applications, as it encompasses a vortex core, carrying a net magnetization which can contribute to heating or serve as a vector for drug delivery [11, 21–26], surrounded by a whirling flux-closure domain, which minimizes stray magnetic fields, thereby preventing undesired magnetic aggregation [27, 28]. Particularly, the morphology of NFs offers a defect-rich, structurally tailorable platform via the grain size [10, 29], where the influence of intra-particle defects into the heating response can be determined.

\* elizabeth.jefremovas@uni.lu

In this work, we capture the heat generation of several NFs of different particle and grain size, evaluating their heating performance measured under AC fields within the range of MHT clinical conditions. Guided by these experiments, we reproduce the realistic morphology of NFs and investigate their dynamics within the micromagnetic framework. This allows us to link their structural features to the dynamics of the vortex texture and its related macroscopic heat generation. Our simulations elucidate the functional role of spin disorder in the macroscopic heating metrics and resolves the heat generation within individual particles, revealing a heterogeneous landscape of localized “hot spots” quantified at nanometer spatial and nanosecond temporal resolution. Together, our results elucidate the functional role of spin disorder in magnetic heating and establish a direct connection between nanoparticle microstructure, micromagnetic texture, and heat dissipation, providing a mechanistic basis for the rational optimization of magnetic hyperthermia.

## MATERIALS AND METHODS

### A. Experimental methods

Maghemite nanoflowers with the smaller grains (7 nm and 10 nm) were synthesized following a scaled-up version of our previously reported modified solvothermal polyol protocol [29]. Briefly, 4.37 g of iron(III) chloride hexahydrate ( $\text{FeCl}_3 \cdot 6\text{H}_2\text{O}$ ,  $\geq 98\%$ , Sigma–Aldrich) were dissolved in 870 mL of ethylene glycol under magnetic stirring at 100 °C for 1 h. Subsequently, 28.4 g of sodium acetate and poly(vinylpyrrolidone) (PVP,  $M_w \approx 40\,000$ , Sigma–Aldrich) were added to the solution. The amount of PVP was varied to tune the particle size: 90 g were used to obtain nanoflowers with an average diameter of  $\approx 170$  nm, whereas 45 g were used to produce larger particles ( $d \approx 220$  nm). The mixture was stirred for  $\approx 30$  min until complete dissolution of the reagents, yielding a homogeneous precursor solution. The solution was then transferred to a Teflon-lined stainless-steel autoclave (1000 mL capacity) and heated at 200 °C for 16 h. After naturally cooling to room temperature, the resulting particles were magnetically separated and washed several times with ethanol.

The obtained particles were subsequently subjected to an acidic oxidation treatment. First, the particles were washed with 300 mL of nitric acid ( $\text{HNO}_3$ , 65%; Sigma–Aldrich) solution (2 M) and magnetically separated. They were then redispersed in 200 mL of iron(III) nitrate nonahydrate ( $\text{Fe}(\text{NO}_3)_3 \cdot 9\text{H}_2\text{O}$ ,  $\geq 99.95\%$ ; Sigma–Aldrich) solution (0.6 M) and heated at 90 °C for 1 h. After cooling to room temperature, the particles were magnetically separated again, washed with 300 mL of

$\text{HNO}_3$  (2 M), rinsed three times with an acetone/water mixture (30:70 v/v), and finally dried at 50 °C overnight.

Nanoflowers with larger grains (21nm and 25 nm) were synthesized under analogous solvothermal conditions. For particles with an average diameter of  $d = 170$  nm, 10.4 g of  $\text{FeCl}_3 \cdot 6\text{H}_2\text{O}$  and 3.2 g of trisodium citrate dihydrate (99%; Sigma Life Sciences) were dissolved in 320 mL of ethylene glycol ( $\geq 99\%$ , Sigma–Aldrich), followed by the addition of 20 g of sodium acetate trihydrate ( $\geq 99\%$ , Sigma–Aldrich) under magnetic stirring. For larger particles ( $d \approx 250$  nm), 21.62 g of  $\text{FeCl}_3 \cdot 6\text{H}_2\text{O}$  and 6 g of trisodium citrate were dissolved in 376 mL of ethylene glycol, after which 40 g of sodium acetate trihydrate were added. In both cases, the mixtures were vigorously stirred for 30 min, transferred into a Teflon-lined aluminium autoclave (1000 mL), and heated at 200 °C for 16 h. After natural cooling to room temperature, the resulting black precipitate was magnetically separated and washed three times with distilled water by magnetic decantation. The final product was subsequently subjected to the acidic oxidation treatment described above and dried at 50 °C overnight.

Transmission electron microscopy (TEM) was performed to determine the morphology and particle-size distribution of the NFs. X-ray diffraction (XRD) was performed to identify the phase and nanocrystallite (grain) size of the NFs. Further details are included in Supplemental Material S1.

AC magnetometry was performed using a commercial AC magnetometer system (“AC Hyster”, Nanotech Solutions, Spain). The system is designed for characterising liquid nanoparticle samples of 40  $\mu\text{L}$ . Hysteresis loops have been measured for the 4 different NF samples of several diameter and grain sizes:  $d = 170$  nm, with grain sizes of  $g_s = 21$  and 7 nm, and  $d = 220$  and 250 nm, with  $g_s = 10$  and 25 nm, respectively, at three different frequencies,  $f = 10$ , 25, and 100 kHz, with AC field amplitudes from  $\mu_0 h_{AC} = 3.83$  kA/m to 25.81 kA/m *i.e.*, all within the clinical safety limits  $h \cdot f \leq 5$  GA/ms [31, 32].

### B. Numerical methods

#### C. Micromagnetic description of maghemite nanoflowers

Micromagnetic simulations were performed using Mumax3[33]. The NFs were generated starting from a cubic simulation region to which a Voronoi tessellation was applied to divide the volume into discrete regions corresponding to individual material grains [34]. A perfectly spherical geometry with an initial diameter  $d$  was then overlaid on this tessellated cube. Only the grains whose

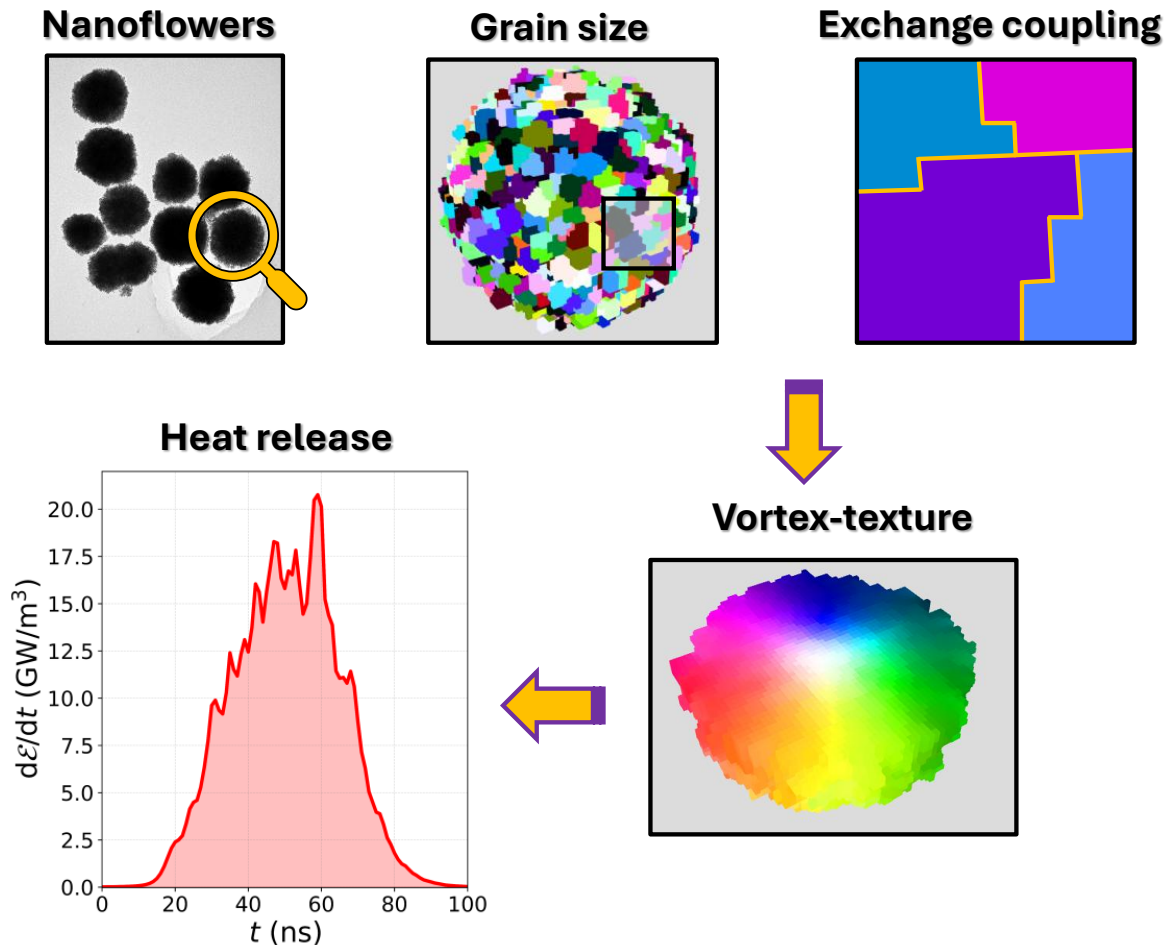


FIG. 1. Iron oxide nanoflowers are multicore aggregates of nanocrystals (commonly referred to as *grains*) of tailorable size with promising prospects in MHT. Our model assigns each grain a random uniaxial anisotropy axis,  $K_u$ , represented by a different colour in the figure. The boundaries in between those grains, highlighted in yellow, are a source of structural and magnetic disorder. We account for them through a reduction of the exchange-coupling at inter-grain boundaries, which together with the grain anisotropy, define the disorder landscape of the NFs. For maghemite NFs above the single-domain threshold ( $d \gtrsim 70$  nm [19, 30]), the magnetic texture folds into a vortex configuration, formed by a vortex core (represented in white) and a perpendicular flux-closure texture (each magnetization direction represented in a different color). In this work, we resolve the heat release under MHT conditions at local scale, with nanometer spatial and nanosecond temporal resolution.

Voronoi centers were located inside the sphere were retained as part of the particle geometry, while grains with centers outside the sphere were removed. This procedure yields a nanoflower-shaped particle composed of multiple irregular grains (see Figure 1). Intra-particle disorder was included by assigning a random uniaxial anisotropy direction  $K_u$  to each grain and by modifying the inter-grain exchange coupling at grain boundaries. Additional details on the simulations are included in the Supplemental Material and Fig. S4 therein.

Critically, we identify both parameters to be controlled by an experimentally-tailorable parameter, the grain size [10, 29], which effectively determines (i) the intra-particle regions sharing the same  $K_u$ ; and (ii) the amount of intra-particle grain boundaries, which determines the pinning landscape. The intra-particle pinning was cap-

tured by modelling the magnetic coupling between adjacent grains via rescaling the exchange parameter  $A$  at the grain boundaries by a factor  $k$  lying between 0 and 1. Material parameters typical for iron oxide were used, including saturation magnetization  $M_s = 400$  kA/m [35, 36], exchange stiffness  $A = 10$  pJ/m [37], uniaxial magnetocrystalline anisotropy  $K_u = 10$  kJ/m<sup>3</sup> [35, 38–40] and Gilbert damping parameter  $\alpha = 0.1$  [41, 42]. A time-dependent magnetic field  $h(t) = h_{AC} \cos(2\pi f t)$  is applied along the  $z$ -axis direction, with  $f = 300$  kHz, to calculate the heat losses per cycle. Using Mumax3, we numerically integrate the Landau-Lifshitz-Gilbert (LLG) equation:

$$\frac{d\mathbf{m}}{dt} = -\frac{\gamma}{1 + \alpha^2} [\mathbf{m} \times \mathbf{B}_{\text{eff}} + \alpha \mathbf{m} \times (\mathbf{m} \times \mathbf{B}_{\text{eff}})], \quad (1)$$

and link the torque exerted on the magnetization to the magnetic energy dissipated via Eq. 2[43]:

$$\frac{d\mathcal{E}}{dt} = \frac{\alpha\gamma M_s}{1 + \alpha^2} (\mathbf{m} \times \mathbf{B}_{\text{eff}})^2 \quad (2)$$

To date, this expression has only been applied to nanoparticles within the macrospin approximation [44, 45]. Our work moves a step forward by applying it to the individual finite-difference cells in the simulation to investigate the heat dissipation in nanoparticles with internal magnetization inhomogeneities, for which large-scale simulations are performed. This dissipated energy can be transformed into the specific loss power or, equivalently, specific absorption rate,  $SAR$ [46] parameter quantifying the heating performance from the hysteresis losses, via:

$$SLP = \frac{f}{\rho} \mu_0 \oint M(H) dH, \quad (3)$$

and thus:

$$SLP = \frac{f}{\rho} \mu_0 \oint M(H) dH = \frac{f}{\rho} \mathcal{E}_{\text{cycle}}^{(V)} \quad (4)$$

Being  $\rho$  the density of the material, which for the present case of maghemite, is  $\rho = 4.9 \text{ g/cm}^3$  [47].

## RESULTS AND DISCUSSION

To link microstructural disorder to heat generation under magnetic hyperthermia conditions, we identify the grain size,  $g_s$ , as the most relevant physical control parameter. From a micromagnetic perspective, this parameter determines the amount of constituent grains,  $N$ , balancing thus both the role of inter-grain pinning boundaries and anisotropy disorder into the magnetization dynamics and heat generation. From an experimental perspective, the grain size can be precisely controlled via growth conditions at fixed nanoflower size [25, 48, 49], thereby enhancing the applicability of our conclusions. Our study combining experimental and simulation results provides unprecedented insights to the intra-particle mechanisms governing the heat generation, capturing the physics underneath the experimental observations.

### GRAIN SIZE IMPACT ON HEAT GENERATION: EXPERIMENTAL EVIDENCE

AC hysteresis loops measurements were performed in four different ensembles of nanoflowers with diameter  $d$  and grain size  $g_s$ :  $(d, g_s) = (170, 21), (170, 7), (220, 10)$  and  $(250, 25)$  nm, from which

the Specific Absorption Rate ( $SAR$ ) was extracted from the associated hysteresis losses (see Supplemental Material Figure S2) via:

$$SAR = \frac{f}{c} \cdot A = \frac{f}{c} \cdot \mu_0 \oint M_t dH_t \quad (5)$$

where  $M_t$  is the instantaneous magnetization at time  $t$ ,  $H_t$  denotes the sinusoidal magnetic field of frequency  $f$  at time  $t$ , and  $c$  is the magnetic material weight concentration in the dispersing medium. These four ensembles of NFs constitute two representative pairs of NFs with similar diameter and different grain size, all being within the same magnetic regime, where the magnetization reversal is dominated by the flux-closure moments [19].

Figure 2 (A)-(C) displays the  $SAR$  as a function of the field amplitude  $h_{AC}$  for the three measured excitation frequencies  $f$ . For the samples with larger grain size, a clear  $SAR$  signal develops for  $h_{AC} \gtrsim 10.11 \text{ kA/m}$ , increasing nearly linearly with  $h_{AC}$  and  $f$  over a broad range. For  $f = 10$  and  $25 \text{ kHz}$ , the  $SAR(h_{AC})$  curves start to bend above  $h_{AC} \gtrsim 19.53 \text{ kA/m}$ , indicating a progressive approach to  $SAR$  saturation. In contrast, at the highest frequency,  $f = 100 \text{ kHz}$ , the response remains far from saturation within the explored field window, implying substantial headroom for further improving performance at higher field amplitudes and frequencies. A linear extrapolation of the  $f = 100.0 \text{ kHz}$  data beyond  $h_{AC} = 19.53 \text{ kA/m}$  suggests that  $SAR \cong 200 \text{ W/g}$  could be reached at  $h_{AC} = 39.79 \text{ kA/m} \cong 50 \text{ mT}$  (see Supplemental Material Figure S3), a value comparable to that reported for commercial  $40 \text{ nm}$  NFs at  $f = 130 \text{ kHz}$  in Ref. [11].

This result is particularly encouraging from the perspective of clinical translation [50]. Above  $d = 70 \text{ nm}$ , the magnetization of the NFs is expected to fold into a vortex configuration [19, 51]. Such a magnetic texture strongly suppresses stray fields, significantly reducing the tendency of magnetic nanoparticles to agglomerate. Since particle agglomeration is known to critically deteriorate heating performance in *in vivo* environments [23, 28, 45, 52], the fact that vortex-state NFs can sustain heating efficiencies comparable to those of smaller single-domain particles represents a highly desirable scenario: efficient heat generation combined with potentially improved colloidal stability under physiological conditions.

On the other hand, samples with smaller grain sizes exhibit almost negligible  $SAR$  at low  $f$ . Only for  $f = 100 \text{ kHz}$  does the  $220 \text{ nm}$  sample with  $g_s = 10 \text{ nm}$  develop a measurable  $SAR$  signal above  $h_{AC} = 10.11 \text{ kA/m}$ , which nevertheless remains nearly seven times smaller than the values obtained for the  $(250, 25)$  nm or  $(170, 21)$  nm NFs. This behaviour suggests that, for small grain sizes, the intra-particle magnetic configuration is

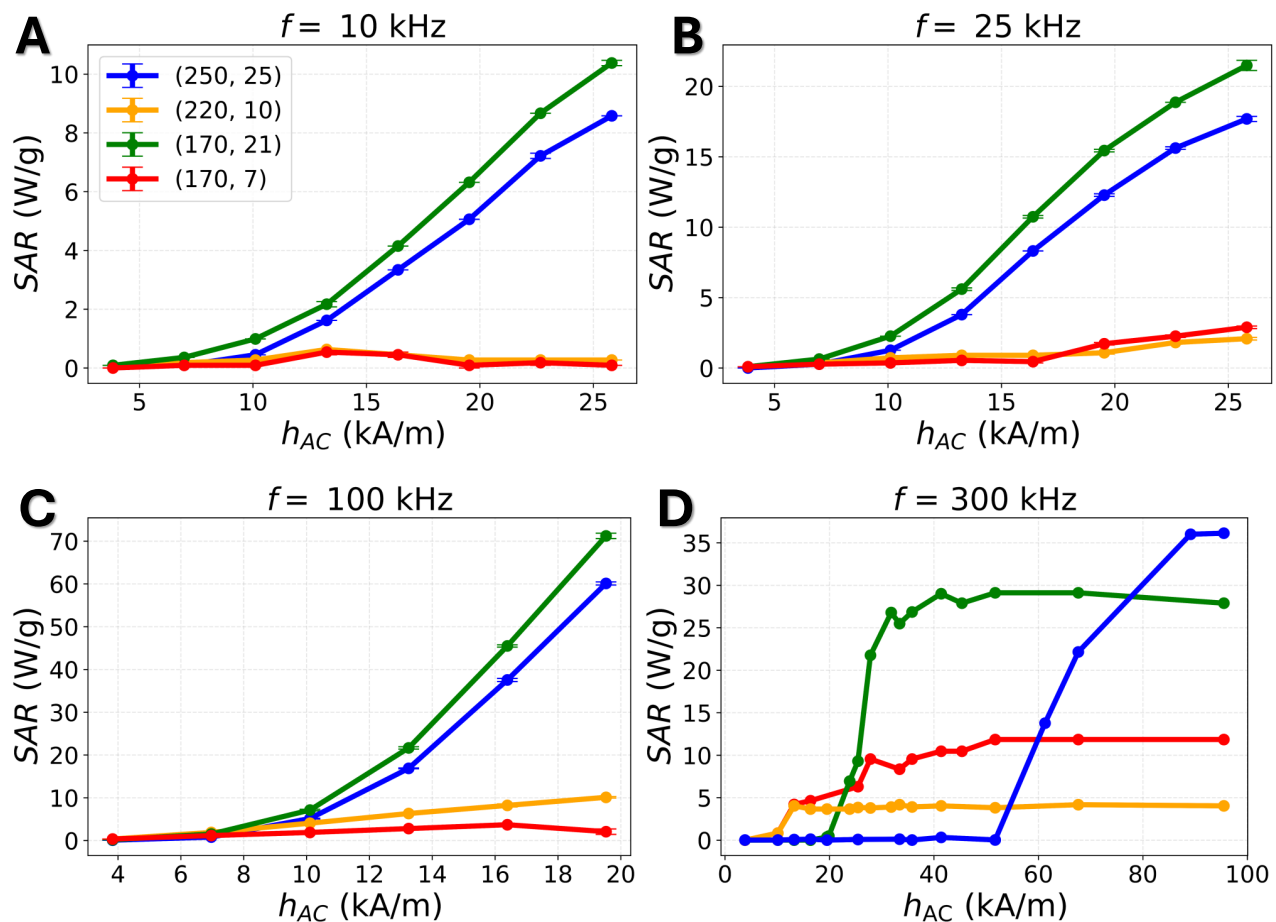


FIG. 2. Specific absorption rate,  $SAR$ , vs. field intensity  $h_{AC}$ , for the 4 NF ensembles measured at **a)**  $f = 10$ , **b)**  $f = 25$ , and **c)**  $f = 100$  kHz. In all cases, the NF with the smaller grain sizes display almost negligible  $SAR$  throughout the explored field range. **d)** Numerical results of the corresponding  $(d, g_s)$  realizations at  $f = 300$  kHz. The simulations are consistent with the experiments: NFs with larger grains generate more heat than their smaller grain counterparts.

characterized by stronger pinning, effectively leading to larger energy barriers for magnetization reconfiguration. This interpretation is consistent with the observation that larger  $f$  and  $h_{AC}$  are required to overcome these barriers and trigger a measurable heat release in NFs with smaller grains. Micromagnetic simulations will further shed light on the microscopic origin of this behaviour.

To elucidate these experimental observations, we performed micromagnetic simulations mimicking the experimental conditions by calculating the heat release per cycle over magnetic fields ranging from  $h_{AC} = 3.8$  kA/m to  $h_{AC} = 51.7$  kA/m at  $f = 300$  kHz. Figure 2(D) includes our numerical results for 170 nm NFs with 21 and 7 nm grain sizes, together with  $(d, g_s) = (220, 10)$  and  $(250, 25)$  nm. The calculated  $SAR$  values reproduce the experimental trends: NFs composed of larger grains, and thus fewer grain boundaries, exhibit enhanced heat dissipation compared to their small-grain counterparts at the probed fields. Notably, the saturated  $SAR$  is approximately three times larger for  $g_s = 21$  nm

than for  $g_s = 7$  nm, increased to almost 7 times for the 220-250 pairs.

Furthermore, the comparison between experiments and simulations provided in Figure 2 underpins the role of thermal fluctuations. Simulations for 170 nm NFs with 21 nm grains show a threshold  $h_{AC} \approx 24$  kA/m for heat release, approximately twice the experimental value, where  $SAR \geq 7$  W/g is already observed at  $h_{AC} \approx 12.5$  kA/m. The same trend follows for the larger NFs, where a threshold value of  $h_{AC} \approx 60$  kA/m for the 250 nm-sized NFs, above the experimental value of  $h_{AC} \approx 10$  kA/m detected, whereas a reduced one of  $h_{AC} \approx 12$  kA/m for the 220 nm-ones is observed. We ascribe the discrepancy between experimental and numerical results to thermal fluctuations. Indeed, although thermal fluctuations are insufficient to dominate magnetization reversal of such large nanoparticles, they effectively lower energy barriers. When the characteristic barrier-crossing time becomes comparable to the AC-field period, thermally assisted switching be-

comes allowed, giving rise to non-zero energy dissipation.

Our numerical results underscore that the poorer heating metrics of the NFs with smaller grains should be ascribed to intrinsic magnetic arguments, rather than to thermal fluctuations. Both the experiments and simulations consistently showcase a reduced heat generation for NFs with smaller grains. Indeed, the increased density of intra-particle boundaries further elevates the energy barriers, imposing larger field excitations (both amplitude and frequency wise) to overcome intra-particle boundaries and trigger a significant heat release. The increased density of intra-particle boundaries also plays a role in the larger field excitation needed to trigger a *SAR* response in the larger NFs observed in our simulations. The  $(d, g_s) = (250, 25)$  nm NFs double the amount of constituent grains of the  $(d, g_s) = (170, 21)$  nm ones, requiring thus larger field excitation for the onset of the *SAR*, achieving also larger *SAR* at saturation. Indeed, thermal fluctuations, present in the experiments, may assist the switching, lowering the field excitation requirements and, consequently, the threshold for these larger NFs.

Finally, size polydispersity and particle agglomeration may further contribute to discrepancies between experiments and simulations. While our calculations consider heat dissipation from a single NF, experiments probe ensembles at Fe concentrations of  $\sim 2\text{--}4$  mg/cm<sup>3</sup>, corresponding to particle concentrations  $\sim 10^{11}$  NFs/cm<sup>3</sup>. Ensemble effects, including size distributions [53, 54] and interparticle interactions arising from agglomeration [28, 45, 52], are therefore expected to influence the measured heating metrics.

All in all, our results elucidate the key influence of grain size into the heating power of NFs. Nanoparticles with smaller grains provide a small heat generation at the probed fields, whereas their larger grain size counterparts deliver heat comparable to smaller commercial counterparts [11], with the key advantage of being less prompt to agglomeration. In the next sections, we will use micromagnetic simulations to capture the underlying fine balance between inter-grain pinning and anisotropy landscape in the heat release, observing a predominant role of the individual grain anisotropy over the inter-grain pinning boundaries.

### GRAIN SIZE IMPACT ON THE HEAT GENERATION: NUMERICAL STUDY

Our experimental results reveal a key influence of the grain size into the heat dissipation, with a privileged role of larger grains compared to the smaller ones. These results are reproduced by our numerical simulations, indicating the microscopic origin of such effect. We

herein build further on the numerical side to capture the intra-particle mechanisms giving rise to such differences.

To unambiguously evaluate the influence of  $g_s$  on heat generation, we compare NFs with  $d = 170$  nm, whose magnetization dynamics is dominated by flux-closure moments [19], with smaller NFs,  $d = 100$  nm, where the dynamics is instead governed by the magnetic moments within the vortex core [19]. This comparison allows us to extend the conclusions on grain-size effects to the whole vortex regime, beyond the specific flux-closure ensembles investigated experimentally in this work. For completeness, we have included in Supplemental Material Section S5 the cases of  $d = 220$  nm and  $d = 250$  nm, which show qualitatively the same behaviour as  $d = 170$  nm.

Figure 3 includes the results corresponding to  $d = 170$  nm with  $g_s = 7$  and 21 nm, and  $d = 100$  nm with grain sizes  $g_s = 4$  and 15 nm. These provide pairs of realizations with comparable numbers of constituent grains  $N$ . Specifically, the configurations  $(d, g_s) = (100 \text{ nm}, 4 \text{ nm})$  and  $(170 \text{ nm}, 7 \text{ nm})$  comprise similar grain counts, with  $N \simeq 8181$  and  $N \simeq 7500$ , respectively, while the configurations  $(100 \text{ nm}, 15 \text{ nm})$  and  $(170 \text{ nm}, 21 \text{ nm})$  yield  $N \simeq 160$  and  $N \simeq 278$ . The use of comparable grain numbers  $N$  across these size regimes enables to extract and identify the different functional role of intra-particle disorder within the two magnetic dynamics regimes.

Figure 3 includes the  $M_z$  vs.  $H_z$  graphs, together with the corresponding magnetic energy accumulated per AC cycle,  $\mathcal{E}_{\text{acc}}$ . As it can be seen in the colour-coded magnetization, realizations with smaller  $g_s$  showcase a sustained, progressive heat release, over the whole reversal process (see top rows in (A) and (C)), whereas for the larger  $g_s$ , the heat release is concentrated at the extremes of the reversal process (see (B) and (D)), regardless of the vortex core- or flux-closure-dominated regimes. We ascribe the vortex-core pinning at the grains (nanocrystallites) as the main source generating a torque for magnetization reversal, which translates into heat. Smaller grain sizes  $g_s$  imply a larger number of constituent grains  $N$ , which generates a denser and more complex pinning landscape, characterized by a higher density of inter-grain boundaries and a broader distribution of local anisotropy axes, which in turn, enhance the coherence and rigidity of the vortex core. The field-driven motion of a more rigid vortex core through this disordered landscape requires thus increased work against pinning forces, resulting in enhanced instantaneous energy dissipation where the energy generation is determined by the depinning and motion of the vortex core. On the other side, the smaller amount of  $N$  of the larger grains result in a vortex core comparatively fragmented or strongly distorted, and the reversal proceeds through more local,

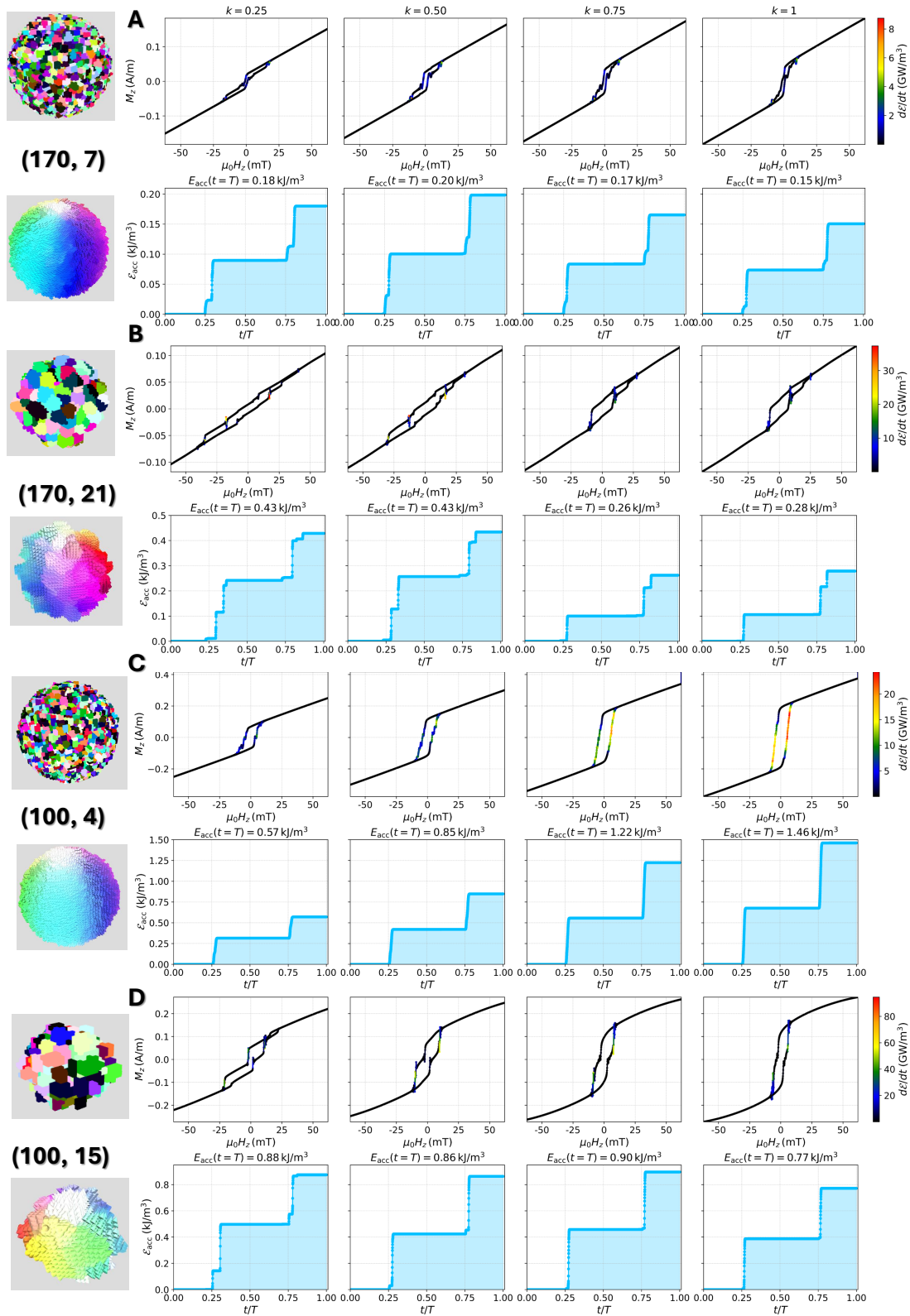


FIG. 3. Magnetization as a function of applied field (top row) and released energy  $\mathcal{E}(t)$  (bottom row) over one AC-field period  $T = 1/300$  ms for NFs with diameters of  $d = 170$  nm and  $g_s = 21$  nm (A) and 7 nm (B), and  $d = 100$  nm and  $g_s = 4$  nm (C) and 15 nm (D). The magnetization traces are colour-coded by the instantaneous heat generation, with red highlighting the points of maximum dissipation, coinciding with the jumps observed in the magnetization consequence of the reversal, *i.e.* moments of maximized torque. The step-like increases in  $\mathcal{E}(t)$  coincide with these dissipation bursts. Sketches represent in top the grain anisotropy, where each colour represents a  $\vec{K}_u$  direction, and the vortex configuration (bottom), where each colour represents a direction of the magnetization.

incoherent rotations, which reduces the net torque and the associated energy dissipation.

The total energy released per cycle,  $\mathcal{E}_{\text{acc}}$ , points consistently to vortex core-dominated realizations to deliver larger values (see bottom rows in (C) and (D)) compared to the flux-closure ones ((A) and (B)). The fact that the magnetization reversal of flux-closure-dominated ensembles occurs partially perpendicular to the  $z$ -direction, whereas the vortex core-dominated follow a reversal path purely along the  $z$ -axis [19] smoothens the torque exerted by the driving field into the magnetization, resulting in a reduced heat generation for the larger flux-closure-dominated NFs. The different magnetization-reversal mechanism (forcing the vortex core to lay perpendicular to the  $z$ -axis, or keeping it purely along the  $z$ -axis) affects the  $\mathcal{E}_{\text{acc}}$  and its dependence on the inter-grain coupling  $k$ . Within the vortex-regime, we detect a systematic increase with  $k$  for  $(d, g_s) = (100 \text{ nm}, 4 \text{ nm})$  (see Figure 3 (A)). In this case, a larger inter-grain exchange coupling yields a more robust and coherent vortex-core profile, which in turn results in an enhanced torque and related energy release. On the contrary, within the flux-closure-dominated regime, the collective dipolar-mediated rotation smoothens the dynamics, weakening the dependence on  $k$ .

### NANOSCALE MAPPING OF INTRA-PARTICLE HEAT GENERATION

Up to this point, we have examined the functional role of intra-particle magnetic disorder into macroscopic parameters, magnetization  $M_z$  and magnetic energy accumulated per AC field cycle,  $\mathcal{E}_{\text{acc}}$ . We herein resolve the heat generation microscopically, identifying the presence of localized ‘‘hot spots’’ at intra-particle level, connecting them to the magnetization reversal stage at nanosecond time resolution.

Figure 4 showcases the spatial distribution of the local heat release at nanometer resolution, at the instant of maximum dissipation for each configuration. In all cases, this moment corresponds to a vortex configuration where the core is oriented perpendicular to the applied field along the  $z$  axis (see 3D magnetization plots in the middle panel of Figure 4), maximizing the instantaneous misalignment between the magnetization and  $\mathbf{B}_{\text{eff}}$  and thus the heat generation. For the NFs with smaller grains, and thus a larger number of constituents, the heat release is spatially distributed over multiple regions, reflecting a complex pinning landscape where the vortex core interacts with numerous grain boundaries and local anisotropy directions. This results in an extended dissipation pattern, consistent with a gradual and sustained reversal process. In contrast, NFs with larger

grains exhibit highly localized and less dense hot spots, indicating a rapid and collective reorientation of the magnetic texture. In this regime, the reduced pinning landscape allows the vortex state to collapse or rotate abruptly once the Zeeman term becomes the dominant factor within the effective field  $B_{\text{eff}}$ , concentrating the dissipation both spatially and temporally.

Figure 4 further includes the instantaneous heat release  $d\mathcal{E}/dt$  vs.  $t$ , along with the visualizations of the heat and magnetization resolved at nanometer resolution (cell size) for  $d = 170$  and  $100 \text{ nm}$  with  $g_s = 7, 21, \text{ and } 4, 15 \text{ nm}$ , respectively. As it can be observed, the heat release for the smaller grains is sustained over the whole reversal process, which we identified to happen at  $t \sim 100 \text{ ns}$ . The heat release happens for the larger grains however a factor 4 faster,  $t \sim 25 \text{ ns}$ , concentrated at the beginning of the reversal process. Such distinct temporal profiles of the heat release can be traced back to the reversal dynamics through Eq. 2, which relates the instantaneous dissipation rate  $d\mathcal{E}/dt$  to the  $(\mathbf{m} \times \mathbf{B}_{\text{eff}})^2$  term. This term reflects the phase lag between the particle magnetization and the  $B_{\text{eff}}$  imposed by the driving AC field, from which the heating originates. In NFs with smaller grains, *i.e.*, larger amount of intra-particle boundaries  $N$ , the dense and heterogeneous pinning landscape prevents rapid alignment of the magnetization with the effective field, sustaining moderate but nonzero values of  $(\mathbf{m} \times \mathbf{B}_{\text{eff}})^2$  over an extended time interval. As a consequence, the heat is released gradually throughout the reversal process, as indicated in the  $M$  vs.  $B_{\text{ext},z}$  plots included in Fig. 3. In contrast, NFs with larger grains offer a reduced pinning landscape, which reduces the rigidity of the vortex core. As a result, the strong initial misalignment of the vortex core with  $\mathbf{B}_{\text{eff}}$  can be easily corrected, delivering a large value of the torque  $(\mathbf{m} \times \mathbf{B}_{\text{eff}})$  over a short time interval. Following Eq. 2, this leads to an intense but shorter dissipation of energy, followed by a negligible contribution once the magnetization realigns with the effective field. It is also worth mentioning the striking differences that intra-particle magnetic disorder introduces to the heat generation distribution, in both space and time domains. Figure S7 in Supplemental Material includes the calculated heat generation of a perfect  $d = 50 \text{ nm}$  single-domain nanospheres. As observed, the heat release occurs at faster pace (within 5 nanoseconds) and spreads over the whole particle, which contrast to the case of the NFs, for which the grain anisotropy delays the heat release and the vortex magnetization concentrates the heat release at the vortex core.

The maximum value of the instantaneous heat release further reflects the interplay between reversal dynamics and internal microstructure. Among the systems studied, the largest peak values of  $d\mathcal{E}/dt$  are observed for the  $(100 \text{ nm}, 15 \text{ nm})$  and  $(170 \text{ nm}, 21 \text{ nm})$  cases,

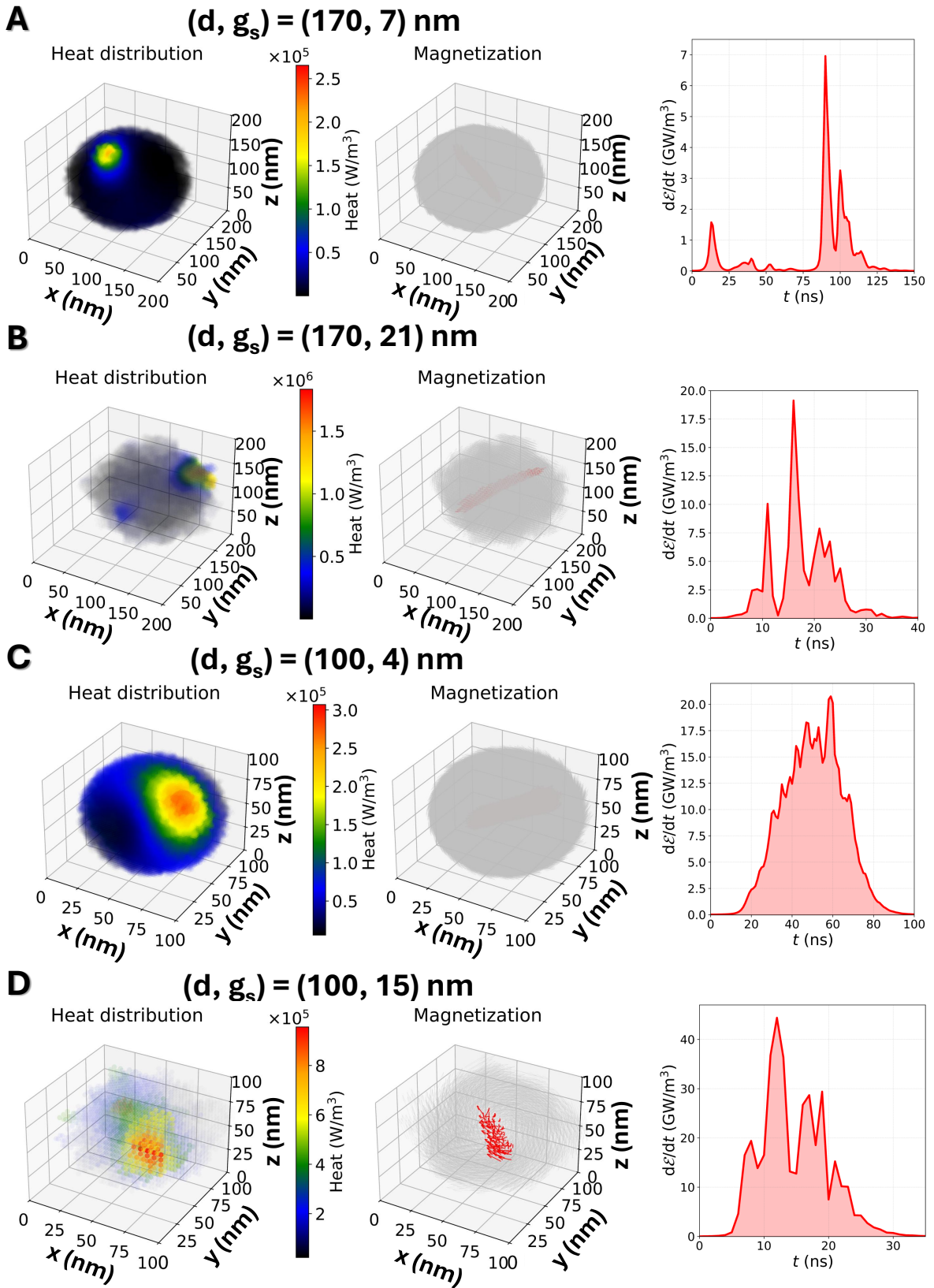


FIG. 4. 3D mappings of heat generation together with the corresponding 3D magnetization configurations and instantaneous heat release  $d\mathcal{E}/dt$  as a function of time for  $(d, g_s) = (170, 7)$ ,  $(170, 21)$ ,  $(100, 4)$  and  $(100, 15)$  nm ((A)–(D), respectively). In all cases the intergrain exchange coupling parameter is fixed to  $k = 1$ , and the external alternating magnetic field is applied at an amplitude of  $\mu_0 h = 62$  mT and frequency  $f = 300$  kHz. The colour bar indicates the intensity of the heat release, ranging from black (minimum) to red (maximum). Magnetic moments within the vortex core are shown as red arrows, while flux-closure moments are represented in grey.

while significantly lower maxima are found for the smallest grains (100 nm, 4 nm) and (170 nm, 7 nm), whose maxima are found at  $\cong 10.013 \text{ GW/m}^3$  and  $\cong 7.821 \text{ GW/m}^3$ , a factor 5 and 7 smaller, respectively. This trend highlights that the instantaneous heat release benefits from the abrupt reorganization of the magnetic texture during reversal, yet such abrupt changes are not beneficial for the time-integrated energy release, as showcased in Fig. 3. In fact, slower magnetization dynamics imposed by a richer pinning landscape lead to a sustained heat release distributed over time, rather than to short-lived, intense peaks. Such a temporally extended dissipation is advantageous not only to deliver a larger generated energy per AC cycle, yet it further avoids highly localized power spikes and promotes a more homogeneous and controllable thermal response, which is particularly desirable for magnetic hyperthermia applications [25].

Our heating maps provide direct visual evidence that the internal granular structure governs not only the magnitude but also the spatial and temporal character of the heat release, linking microstructure to reversal dynamics and energy dissipation.

## CONCLUSIONS

In this work, we link microstructural features to macroscopic heating performance by resolving the spatio-temporal magnetization dynamics of iron oxide NFs, thereby connecting intra-particle magnetic defects to heat generation at the particle scale. Starting from the experimental observation that NFs with larger grains deliver better heat release, we use a micromagnetic framework to capture the influence of intra-particle magnetic disorder into the macroscopic heat release, and to localize spatially and temporally the occurrence of “hot spots” at intra-particle level.

By using the grain size as an experimentally controllable parameter, we have determined the crucial influence of structural disorder into the heat generation. Whereas the smaller grains offer a larger collection of inter-grain pinning boundaries, which in principle should on its own deliver a larger energy release, they broaden at the same time the anisotropy landscape, which facilitates core mobility through hopping between local anisotropy directions, highlighting the critical balance between both pinning and anisotropy landscapes. As a result, the smaller grains impose (i) a larger frequency and field amplitudes to trigger a heat release, as observed in the experimental results; and (ii) a heat release that balances the benefits of deeper pinning landscapes with the detrimental effect of weaker anisotropy landscape.

We have shown how nanoflowers with larger grains

within the flux-closure dominated regime deliver heat comparable to smaller commercial counterparts [11], with the key advantage of being less prompt to agglomeration. Samples with smaller grains, despite offering a larger pinning potential in terms of inter-grain boundaries, lose their heating power by offering a smoother anisotropy landscape, highlighting the dominant role of the latter over the inter-grain pinning in the heating response. Furthermore, our experiments allowed to underscore the role of thermal fluctuations, which do not change the qualitative trends, yet they effectively reduce the energy demands on the magnetic field excitation, observing larger heat release at smaller frequency and field amplitudes compared to our micromagnetic athermal simulations.

Our simulations indicate a larger heating performance of vortex core-dominated NFs compared to the flux-closure-dominated counterparts, supporting the  $d = 100 - 120 \text{ nm}$  size windows for the hyperthermia “sweet spot” [19]. Both our experiments and simulations reveal a larger energy dissipated for realizations with smaller grains, consequence of the more dense pinning landscape, providing a guide for the rational design of optimized nanotransducers. Our simulations further highlight larger grains yielding a more localized distribution of “hot spots” in both space and time, whereas smaller grains spread dissipation over broader regions of the particle and over longer time windows. This spatio-temporal resolution provides a practical design handle: it resolves at intra-particle level where heat is generated and for how long the release is sustained, thereby enabling informed choices of microstructure depending on whether rapid, concentrated heating or more distributed, sustained dissipation is desired.

We can anticipate that, for MHT applications, slower magnetization dynamics imposed by a rich pinning landscape leading to a sustained heat release distributed over time is preferred over short-lived, intense peaks. Such transient power spikes may occur too rapidly to effectively disrupt the metabolic activity of tumoral cells, whereas a more gradual heat release promotes a homogeneous and controllable thermal response, which is particularly desirable for magnetic hyperthermia applications.

## ACKNOWLEDGEMENTS

E.M.J. acknowledges funding from the European Union’s Horizon 2020 research and innovation program under the Marie Skłodowska-Curie actions grant agreement No. 101081455-YIA (HYPUSH); the Institute for Advanced Studies (IAS) of the University of Luxembourg; and the Fonds Wetenschappelijk Onderzoek (FWO-Vlaanderen) project number No. V501325N. P. R.

acknowledges Flanders Innovation & Entrepreneurship (Project No. HBC.2022.0682). The PTB guest scientist program giving the opportunity to P. Rooms to carry out AC measurements is kindly acknowledged. COST Action CA23132 “Magnetic Particle Imaging for next-generation theranostics and medical research” (NexMPI), supported by COST (European Cooperation in Science and Technology) is kindly acknowledged. The computational resources and services used in this work were provided by the HPC facilities of the University of Luxembourg, the Luxembourg national supercomputer MeluXina, the VSC (Flemish Supercomputer Center), funded by the Research Foundation Flanders (FWO) and the Flemish Government – department EWI, and the Donostia International Physics Center (DIPC). The authors gratefully acknowledge the HPC UniLu, LuxProvide, VSC and DIPC Supercomputing Center teams for their technical and human support.

## AUTHOR CONTRIBUTIONS STATEMENT

Conceptualization: E.M.J. Methodology: E.M.J., J. L. Software: E.M.J., J.L. Validation: all authors. Formal analysis: E.M.J., P.R. Investigation: E.M.J., P.R. Sample preparation: A.G-C., MP.M. Resources: All authors. Data curation: E.M.J., P.R. Visualization: E.M.J., P.R. Supervision: A. M., F.W., MP.M., J.L. Project administration: E.M.J., A.M., J.L. Funding acquisition: E.M.J. Writing original draft: E.M.J. Writing, review, and editing: all authors.

## COMPETING INTERESTS

The authors declare no competing interests. The corresponding author is responsible for submitting a [competing interests statement](#) on behalf of all authors of the paper. This statement must be included in the submitted article file.

- 
- [1] K. Wu, J.-P. Wang, N. A. Natekar, S. Ciannella, C. González-Fernández, J. Gomez-Pastora, Y. Bao, J. Liu, S. Liang, X. Wu, *et al.*, *Nanotechnology* (2024).
- [2] Q. Pankhurst, N. Thanh, S. Jones, and J. Dobson, *Journal of Physics D: Applied Physics* **42**, 224001 (2009).
- [3] Q. A. Pankhurst, J. Connolly, S. K. Jones, and J. Dobson, *Journal of physics D: Applied Physics* **36**, R167 (2003).
- [4] M. Colombo, S. Carregal-Romero, M. F. Casula, L. Gutiérrez, M. P. Morales, I. B. Böhm, J. T. Heverhagen, D. Proseri, and W. J. Parak, *Chemical Society Reviews* **41**, 4306 (2012).
- [5] Z. V. Díaz-Riascos, M. Llaguno-Munive, N. Lafuente-Gómez, Y. Luengo, S. Holmes, J. Volatron, O. Ibarrola, S. Mancilla, F. Sarno, J. J. Aguirre, *et al.*, *ACS Applied Materials & Interfaces* (2025).
- [6] E. A. Perigo, G. Hemery, O. Sandre, D. Ortega, E. Garaio, F. Plazaola, and F. J. Teran, *Applied Physics Reviews* **2** (2015).
- [7] A. Rivera-Rodriguez and C. M. Rinaldi-Ramos, *Annual Review of Chemical and Biomolecular Engineering* **12**, 163 (2021).
- [8] H. Gavilán, A. Gallo-Cordova, M. L. R. Chediak, A. P. Rodríguez, M. P. Morales, and L. Gutiérrez, *Nanoscale* , 27734 (2025).
- [9] C. S. Kumar and F. Mohammad, *Advanced drug delivery reviews* **63**, 789 (2011).
- [10] A. Gallo-Cordova, B. Corrales-Pérez, P. Cabrero, C. Force, S. Veintemillas-Verdaguer, J. G. Ovejero, and M. P. Morales, *Chemical Engineering Journal* **490**, 151725 (2024).
- [11] E. M. Jefremovas, L. Gandarias, I. Rodrigo, L. Marcano, C. Grüttner, J. Á. García, E. Garayo, I. Orue, A. García-Prieto, A. Muela, *et al.*, *IEEE Access* **9**, 99552 (2021).
- [12] P. Bender, J. Fock, C. Frandsen, M. F. Hansen, C. Balceris, F. Ludwig, O. Posth, E. Wetterskog, L. K. Bogart, P. Southern, *et al.*, *The Journal of Physical Chemistry C* **122**, 3068 (2018).
- [13] W. Mekseriwattana, N. Silvestri, R. Brescia, E. Tiryaki, J. Barman, F. G. Mohammadzadeh, N. Jarmouni, and T. Pellegrino, *Advanced Functional Materials* **35**, 2413514 (2025).
- [14] A. Riedinger, P. Guardia, A. Curcio, M. A. Garcia, R. Cingolani, L. Manna, and T. Pellegrino, *Nano Letters* **13**, 2399 (2013).
- [15] C. Blanco-Andujar, D. Ortega, P. Southern, S. A. Nesbitt, N. T. K. Thanh, and Q. A. Pankhurst, *Nanomedicine* **11**, 121 (2016).
- [16] A. Lappas, G. Antonaropoulos, K. Brintakis, M. Vasilakaki, K. N. Trohidou, V. Iannotti, G. Ausanio, A. Kostopoulou, M. Abeykoon, I. K. Robinson, *et al.*, *Physical Review X* **9**, 041044 (2019).
- [17] B. G. Prajapati, K. Verma, S. Sharma, and D. U. Kapoor, *Medical Oncology* **41**, 295 (2024).
- [18] L. G. Vivas, R. Yanes, D. Berkov, S. Erokhin, M. Bersweiler, D. Honecker, P. Bender, and A. Michels, *Physical Review Letters* **125**, 117201 (2020).
- [19] E. M. Jefremovas, L. Calus, and J. Leliaert, *Small Science* **6**, e202500490 (2026).
- [20] G. M. Rizzo, N. Silvestri, N. Jarmouni, H. Gavilán, H. Yakubu, D. Arenas-Esteban, S. Bals, P. Parlanti, M. Gemmi, R. C. Prado, *et al.*, *Advanced Functional Materials* , e22732 (2026).
- [21] D. Ho, X. Sun, and S. Sun, *Accounts of Chemical Research* **44**, 875 (2011).
- [22] M. Goiriena-Goikoetxea, A. García-Arribas, M. Rouco, A. Svalov, and J. Barandiaran, *Nanotechnology* **27**, 175302 (2016).
- [23] M. Goiriena-Goikoetxea, D. Muñoz, I. Orue, M. Fernández-Gubieda, J. Bokor, A. Muela, and A. García-Arribas, *Applied Physics Reviews* **7** (2020).
- [24] N. Usov, M. Nesmeyanov, and V. Tarasov, *Scientific Reports* **8**, 1224 (2018).
- [25] H. Gavilán, S. K. Avugadda, T. Fernández-Cabada, N. Soni, M. Cassani, B. T. Mai, R. Chantrell, and T. Pel-

- legrino, *Chemical Society Reviews* **50**, 11614 (2021).
- [26] P. Hugounenq, M. Levy, D. Alloyeau, L. Lartigue, E. Dubois, V. Cabuil, C. Ricolleau, S. Roux, C. Wilhelm, F. Gazeau, *et al.*, *The Journal of Physical Chemistry C* **116**, 15702 (2012).
- [27] D. Serantes and D. Baldomir, *Nanomaterials* **11**, 2786 (2021).
- [28] M. L. Etheridge, K. R. Hurley, J. Zhang, S. Jeon, H. L. Ring, C. Hogan, C. L. Haynes, M. Garwood, and J. C. Bischof, *Technology* **2**, 214 (2014).
- [29] H. Gavilán, E. H. Sánchez, M. E. F. Brollo, L. Asín, K. K. Moerner, C. Frandsen, F. J. Lázaro, C. J. Serna, S. Veintemillas-Verdaguer, M. P. Morales, and L. Gutiérrez, *ACS Omega* **2**, 7172 (2017).
- [30] G. Di Fratta, C. Serpico, and M. d’Aquino, *Physica B* **407**, 1368 (2012).
- [31] R. Hergt and S. Dutz, *Journal of Magnetism and Magnetic Materials* **311**, 187 (2007).
- [32] R. Hergt, S. Dutz, and M. Zeisberger, *Nanotechnology* **21**, 015706 (2009).
- [33] A. Vansteenkiste, J. Leliaert, M. Dvornik, M. Helsen, F. Garcia-Sanchez, and B. Van Waeyenberge, *AIP Advances* **4**, 107133 (2014).
- [34] J. Leliaert, B. Van de Wiele, A. Vansteenkiste, L. Laurson, G. Durin, L. Dupré, and B. Van Waeyenberge, *Journal of Applied Physics* **115**, 233903 (2014).
- [35] A. G. Roca, J. F. Marco, M. P. Morales, and C. J. Serna, *The Journal of Physical Chemistry C* **111**, 18577 (2007).
- [36] H. Shokrollahi, *Journal of Magnetism and Magnetic Materials* **426**, 74 (2017).
- [37] E. P. Sinaga, M. P. Adams, E. H. Hasdeo, and A. Michels, *Physical Review B* **110**, 054404 (2024).
- [38] B. Gross, S. Philipp, E. Josten, J. Leliaert, E. Wetterskog, L. Bergström, and M. Poggio, *Physical Review B* **103**, 014402 (2021).
- [39] J. Borchers, K. Krycka, B. Bosch-Santos, E. de Lima Correa, A. Sharma, H. Carlton, Y. Dang, M. Donahue, C. Grüttner, R. Ivkov, *et al.*, *Small Structures* **6**, 2400410 (2025).
- [40] K. Pisane, S. Singh, and M. Seehra, *Applied Physics Letters* **110** (2017).
- [41] P. Allia and P. Tiberto, *Journal of Nanoparticle Research* **13**, 7277 (2011).
- [42] N. Çam, I. López-Vázquez, Ò. Iglesias, and D. Serantes, arXiv preprint arXiv:2601.20315 (2026).
- [43] C. Muñoz-Menendez, D. Serantes, O. Chubykalo-Fesenko, S. Ruta, O. Hovorka, P. Nieves, K. Livesey, D. Baldomir, and R. Chantrell, *Physical Review B* **102**, 214412 (2020).
- [44] J. Leliaert, J. Ortega-Julia, and D. Ortega, *Nanoscale* **13**, 14734 (2021).
- [45] J. Ortega-Julia, D. Ortega, and J. Leliaert, *Nanoscale* **15**, 10342 (2023).
- [46] Although a distinction between *SLP* (intrinsic heat generation) and *SAR* (experimental quantification of heat generation) is sometimes distinguished on conceptual grounds, both metrics are conceptually equivalent and quantify the same underlying heating process. Their formulation differs only in their normalization factor, with *SAR* defined per mass concentration in the medium ( $c$ ) and *SLP* per intrinsic material density ( $\rho$ ).
- [47] J. A. R. Guivar, A. I. Martínez, A. O. Anaya, L. D. L. S. Valladares, L. L. Félix, and A. B. Dominguez, *Advances in Nanoparticles* **2014** (2014).
- [48] H. Gavilán, E. H. Sánchez, M. E. Brollo, L. Asín, K. K. Moerner, C. Frandsen, F. J. Lázaro, C. J. Serna, S. Veintemillas-Verdaguer, M. P. Morales, *et al.*, *ACS Omega* **2**, 7172 (2017).
- [49] H. Gavilán, K. Simeonidis, E. Myrovali, E. Mazarío, O. Chubykalo-Fesenko, R. Chantrell, L. Balcells, M. Angelakeris, M. P. Morales, and D. Serantes, *Nanoscale* **13**, 15631 (2021).
- [50] L. Beola, L. Asín, C. Roma-Rodrigues, Y. Fernández-Afonso, R. M. Fratila, D. Serantes, S. Ruta, R. W. Chantrell, A. R. Fernandes, P. V. Baptista, *et al.*, *ACS Applied Materials & Interfaces* **12**, 43474 (2020).
- [51] C. Moya, M. Escoda-Torroella, J. Rodríguez-Álvarez, A. I. Figueroa, Í. García, I. B. Ferrer-Vidal, A. Gallo-Cordova, M. P. Morales, L. Aballe, A. F. Rodríguez, *et al.*, *Nanoscale* **16**, 1942 (2024).
- [52] C. Guibert, V. Dupuis, V. Peyre, and J. Fresnais, *The Journal of Physical Chemistry C* **119**, 28148 (2015).
- [53] M. Jeun, S. Bae, A. Tomitaka, Y. Takemura, K. H. Park, S. H. Paek, and K.-W. Chung, *Applied Physics Letters* **95** (2009).
- [54] A. P. Khandhar, R. M. Ferguson, and K. M. Krishnan, *Journal of applied physics* **109** (2011).

# Supplemental Material to: Nanoscale mapping of internal magnetization dynamics reveals how disorder shapes heat generation in magnetic particle hyperthermia

Elizabeth M Jefremovas,<sup>1,2,\*</sup> Pauline Rooms,<sup>3</sup> Álvaro Gallo-Córdova,<sup>4</sup> María P. Morales,<sup>4</sup> Frank Wiekhorst,<sup>5</sup> Andreas Michels,<sup>1</sup> and Jonathan Leliaert<sup>3</sup>

<sup>1</sup>*Department of Physics and Materials Science,  
University of Luxembourg, 162A Avenue de la Faiencerie,  
L-1511 Luxembourg, Grand Duchy of Luxembourg*

<sup>2</sup>*Institute for Advanced Studies, University of Luxembourg,  
Campus Belval, L-4365 Esch-sur-Alzette, Luxembourg*

<sup>3</sup>*DyNaMat, Department of Solid State Sciences,  
Ghent University, 9000 Ghent, Belgium*

<sup>4</sup>*Instituto de Ciencia de Materiales de Madrid (ICMM-CSIC), Madrid 28049, Spain*

<sup>5</sup>*Physikalisch-Technische Bundesanstalt, D-10587 Berlin, Germany*

(Dated: March 17, 2026)

## Abstract

This Supplemental Material includes the structural characterization of the experimentally measured nanoflowers (transmission electron microscopy and X-ray diffraction); extended discussions on the validity of our simulations without thermal noise; experimental AC hysteresis loops, from which the  $SAR$  is extracted; a linear extrapolation of the experimentally-measured  $SAR$  at  $f = 100$  kHz; temperature mappings and heat release for  $(d, g_s) = (220, 10)$  and  $(250, 25)$  nm; and temperature mappings, heat release and magnetization reversal of a representative single-domain spherical nanoparticle.

### S1. STRUCTURAL CHARACTERIZATION

Transmission electron microscopy (TEM) was performed using a JEOL JEM 1010 electron microscope at an accelerating voltage of 100 kV. For sample preparation, a diluted suspension of NFs was deposited onto an amorphous 300 micron meshed carbon-coated copper grid, followed by evaporation at room temperature. The particle-size distribution was analyzed using the standard software ImageJ [1] for digital electron microscope image processing, assimilating the particle diameter as the largest internal dimension. Data for an approximate number of at least 200 particles were acquired and fitted to a lognormal distribution, allowing for the calculation of the mean particle size and characterization of the particle size distribution. Figure S1 includes representative TEM images together with the corresponding statistical results for mean particle size, included also in Table S S1.

To identify the phase and crystalline structure of the NFs, X-ray diffraction (XRD) measurements were performed using a Bruker D8 Advance diffractometer equipped with a graphite monochromator and a Cu-K $\alpha$  source ( $\lambda = 1.5406$  Å). The XRD patterns were recorded at room temperature and ambient pressure in the  $2\theta$  range from  $20^\circ$  to  $70^\circ$ . The results, that can be inspected in Figure S1, where the most intense peaks have been indexed according to their Miller indices, confirm a single spinel iron-oxide phase, consistent with  $\gamma$ -Fe<sub>2</sub>O<sub>3</sub>/Fe<sub>3</sub>O<sub>4</sub>. Considering the post-synthetic oxidative treatment, the phase is assigned to maghemite. To estimate the mean crystal size, corresponding to the size of the grains,

---

\* [elizabeth.jefremovas@uni.lu](mailto:elizabeth.jefremovas@uni.lu)

Scherrer’s equation was used [2],

$$D = \frac{K \lambda}{\beta \cos \theta} \quad (1)$$

where  $K$  is typically taken as 0.9 for nanoparticles and  $\beta$  represents the full width at half-maximum of the most intense peak, which in our case corresponds to the (3 1 1) reflection. The results for grain size are also included in Table S S1.

TABLE S1. Structural parameters of the studied samples: Mean diameter  $\langle d \rangle$  and corresponding standard deviation  $\sigma$ , and grain size  $g_s$ .

Sample	$\langle d \rangle$ (nm)	$\sigma$ (nm)	$g_s$ (nm)
(170, 21)	170	40	21
(170, 7)	168	51	7
(250, 25)	250	20	25
(220, 10)	220	30	10

## S2. MAGNETIC FLUID HYPERTHERMIA EXPERIMENTAL MEASUREMENTS

In order to determine experimentally the heating efficiency of the nanoflowers, we have performed AC hysteresis loops measurements and calculated their Specific Absorption Rate ( $SAR$ ) from the hysteresis losses associated. The AC hysteresis loops have been measured for 4 different NF samples of several diameter and grain sizes:  $d = 170$  nm, with grain sizes of  $g_s = 21$  and 7 nm, and  $d = 220$  and 250 nm, with  $g_s = 10$  and 25 nm, respectively. The AC loops have been measured at three different frequencies,  $f = 10, 25,$  and 100 kHz, with AC field amplitudes from  $h_{AC} = 3.83$  kA/m to 25.81 kA/m *i.e.*, all within the clinical safety limits  $h \cdot f \leq 5$  GA/ms [3, 4]. These loops are included in Fig. S2, where it can be seen how the AC loops become wider at increasing the field amplitude  $h_{AC}$ , evolving from the narrow and elongated lancet shape at low fields, with low hysteresis losses and associated heating efficiencies, to wider and square-like loops of increasing heat losses.

A more insightful comparison emerges when contrasting samples with smaller grain sizes ( $g_s = 7$  and 10 nm) to those with larger grains ( $g_s = 21$  and 25 nm). While the former exhibit

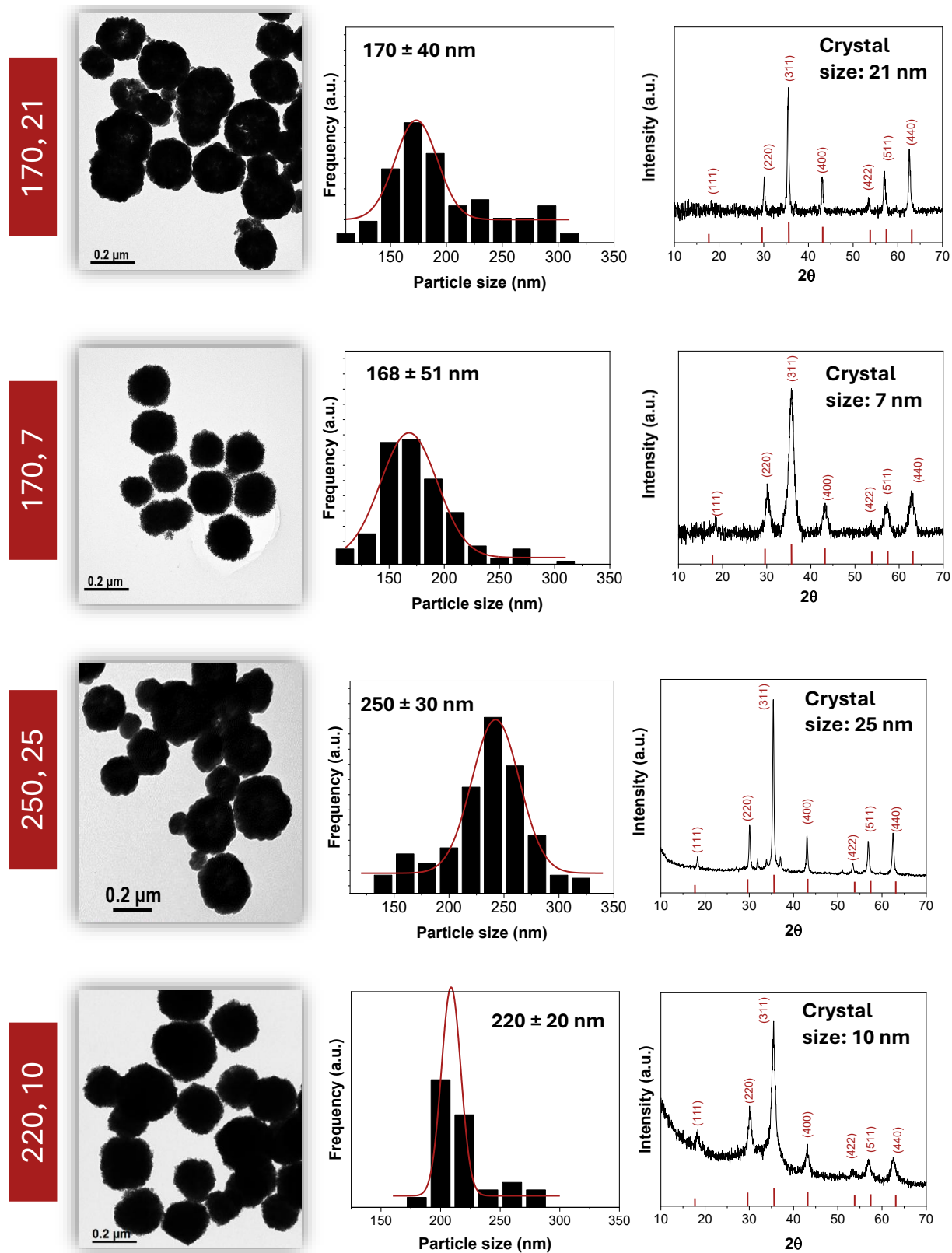


FIG. S1. Representative TEM images, for the four different batches of NFs, along with their size distribution analysis, fitted to a log-normal distribution, and XRD patterns.

no measurable coercivity under any tested field amplitude or frequency, the latter progressively develop broader and more square-shaped hysteresis loops, reaching  $\mu_0 H_c \cong 6.3$  mT at applied fields of 16.39 kA/m for  $f = 10.0$  kHz and 19.53 kA/m for  $f = 100.0$  kHz. This behaviour is illustrated in Fig. S2, where we show the loops acquired at  $h_{AC} = 19.53$  kA/m for all four samples across several frequencies.

As seen in the figure, the samples with  $g_s = 21$  and 25 nm display nearly identical hysteresis loop shapes: wide, square loops with  $\mu_0 H_c \cong 6.3$  mT and maximum magnetization values of  $M \cong 40$  A m<sup>2</sup> kg<sup>-1</sup>, exhibiting only minor frequency dependence. In contrast, samples with  $g_s = 7$  and 10 nm generate loops with almost negligible coercivity. Their maximum magnetization also differs: for particles of  $d = 220$  nm, the saturation magnetization is approximately 1.2 times higher than in the  $d = 170$  nm nanoflowers.

At the highest measured frequency,  $f = 100$  kHz, the small-grain samples display only a marginal coercivity of  $\mu_0 H_c \cong 1$  mT and 0.2 mT, respectively. This indicates that such small grains do not efficiently activate hysteresis losses at sub-hundred-kilohertz frequencies.

### S3. EXTRAPOLATION OF $SAR$ AT HIGHER $h_{AC}$ AMPLITUDES

Figure S3 includes the experimental data, together with linear fits performed in the linear regime ( $h_{AC} \geq 13.25$  kA/m), for  $(d, g_s) = (250, 25)$  and  $(170, 21)$  NFs. A  $SAR$  value of  $\approx 231$  W/g and  $\approx 199$  W/g is estimated, similar to the one obtained for an ensemble of single-domain NFs ( $d = 45$  nm), as reported in Ref. [5], yet with a concentration 1.5 smaller for the present study.

### S4. VALIDITY OF SIMULATIONS WITHOUT THERMAL NOISE

Our micromagnetic simulations under frequency-dependent AC magnetic fields were performed without explicitly including a stochastic thermal field associated with finite-temperature fluctuations. This choice is motivated by computational feasibility and by the physical regime addressed in this work. Incorporating a thermal noise term within stochastic Landau–Lifshitz–Gilbert dynamics would dramatically increase the computational cost of

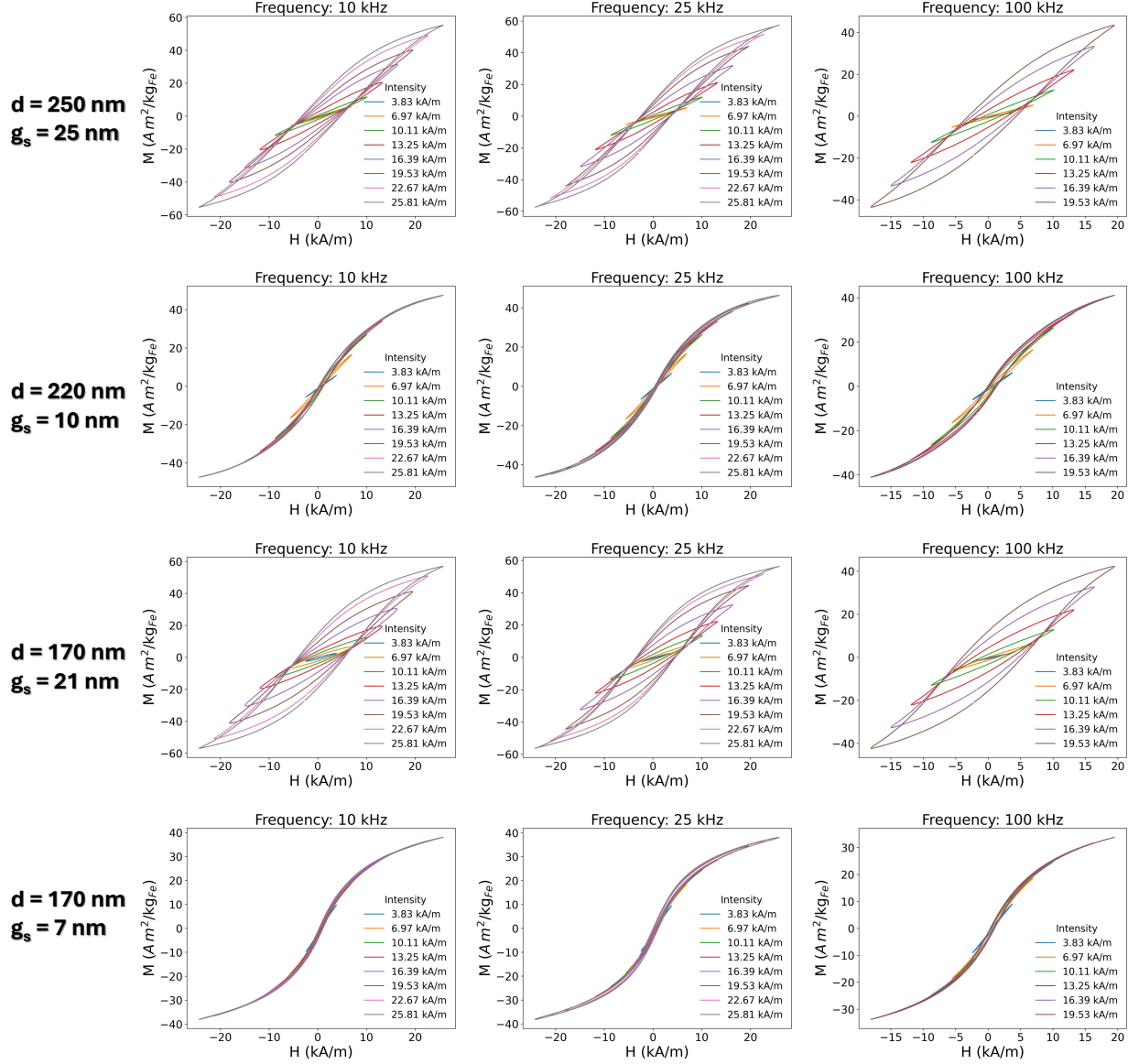


FIG. S2. AC hysteresis loops measured for the NFs with  $d = 250, 220$  and  $170$  nm with grain sizes of  $g_s = 25, 10, 21$  and  $7$  nm (top to bottom), at  $f = 10, 25$  and  $100$  kHz, with AC field amplitudes up to  $h_{AC} = 25.81$  kA/m, respectively.

the large-scale parametric study presented here, while providing limited additional insight into the dominant magnetization-reversal mechanisms and energy dissipation processes of interest.

The nanoflowers considered in this study are well above both the superparamagnetic and

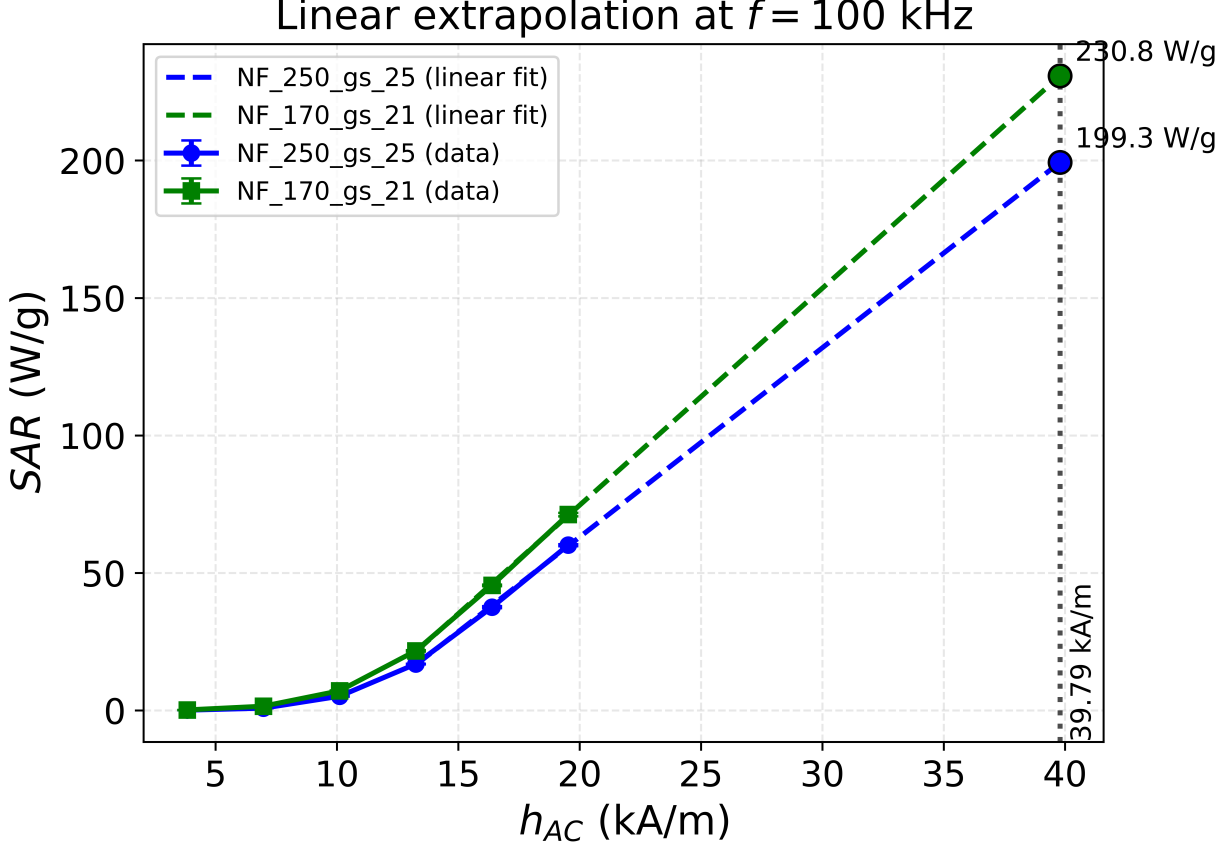


FIG. S3. Specific absorption rate (SAR) as a function of the AC field amplitude  $h_{AC}$  at  $f = 100$  kHz for  $(d, gs) = (250, 25)$  nm and  $(170, 21)$  NFs. Symbols denote experimental data, while dashed lines correspond to linear fits performed in the linear regime ( $h_{AC} \geq 13.25$  kA/m). Filled markers indicate extrapolated SAR values at  $h_{AC} = 39.79$  kA/m ( $\approx 50$  mT).

single-domain limits. The superparamagnetic diameter can be estimated as

$$d_{\text{SPM}} \approx \left( \frac{6 \cdot 25 \cdot k_B T}{\pi K_u} \right)^{1/3} \approx 27 \text{ nm},$$

assuming  $\tau = \tau_0 \exp(K_u V / k_B T)$  with  $\ln(\tau / \tau_0) = 25$  at room temperature [6]. The single-domain limit can be approximated as  $d_{\text{SD}} \approx 7.2 l_{\text{ex}}$  [7], corresponding to  $\sim 51$  nm for maghemite nanoflowers [8]. Within the investigated size range and excitation frequencies (10–300 kHz), the magnetization dynamics is therefore neither governed by Néel nor by Brownian relaxation. Instead, the response evolves from thermally assisted diffusion at low fields to field-induced crossing of energy barriers at larger amplitudes, resulting in a hysteretic regime [9–12], where heat release is primarily driven by the applied field with minor influence of thermal fluctuations on the absolute figures.

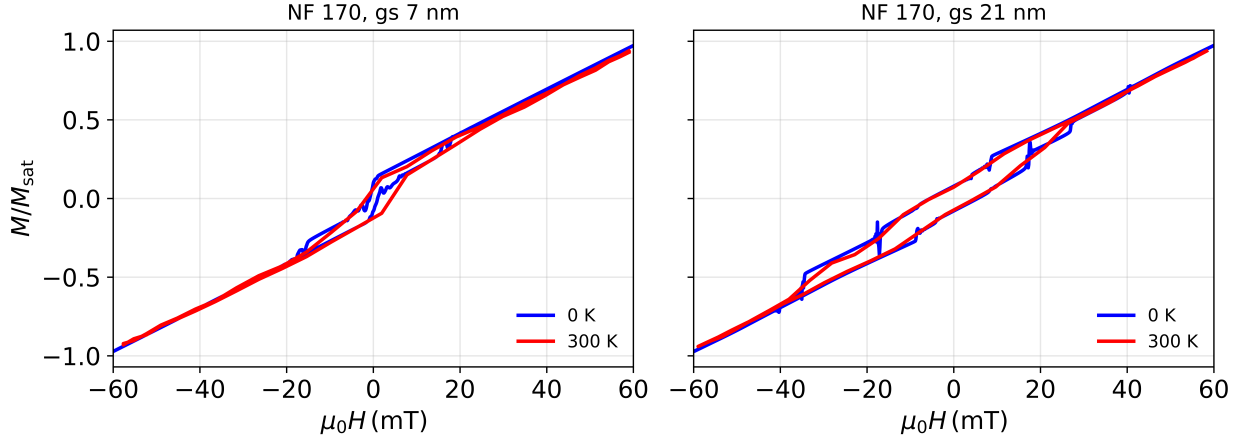


FIG. S4. Hysteresis loops calculated for  $d = 170$  nm NFs with  $g_s = 7$  and  $21$  nm, respectively, at  $T = 0$  K and  $300$  K. Driving field parameters are  $f = 300$  kHz and  $h_{AC} = \pm 49.33$  kA/m. No significant changes in the coercivity are observed.

To assess the impact of finite temperature on the extracted energy losses, we directly compared hysteresis loops obtained from simulations performed at  $T = 0$  K and  $T = 300$  K, with AC field excitation of  $f = 300$  kHz and maximum field amplitude of  $h_{AC} = \pm 49.33$  kA/m. Figure S4 presents averaged loops (10 realizations) for NFs of  $d = 170$  nm, combined with grain sizes of  $g_s = 7$  nm and  $21$  nm. In all cases, the loops display a similar qualitative behaviour: in the loops at  $T = 0$  K, the magnetization exhibits some jumps, revealing the pinning of the vortex core at the inter-grain boundaries while the magnetization reversal takes place. Those jumps are suppressed at  $T = 300$  K, where the thermal fluctuations provide an extra energy to overcome the pinning energy barriers, resulting in a smoother magnetization reversal with no pinning. However, the loop coercivity remains almost constant at both temperature values, constraining the effect of thermal fluctuations to the magnetization dynamics, yet with little to negligible effect on the macroscopic magnetic energy stored per cycle. This demonstrates that the dominant dissipation mechanism is field-driven, with minimal influence of thermal effects at the proven fields.

## S5. SIMULATIONS FOR LARGER NFS: $d = 220$ NM AND $250$ NM

Figures S5 and S6 include the results corresponding to  $(d, gs) = (220, 10)$  and  $(250, 25)$  NFS. Akin to the simulations shown in the main text, the heat release is concentrated at the extremes of the magnetization reversal. The energy accumulated per cycle a factor 6 larger for the larger grains compared to the smaller counterparts, in agreement with the simulations for  $d = 170$  nm and the experimental results. The heat release of the NFS with smaller grains  $(220, 10)$  is concentrated spatially around the vortex core, extending over a longer period of time ( $t \sim 100$  ns) compared to the realizations with larger grains  $(250, 25)$ , which deliver the heat at a shorter time windows ( $t \sim 25$  ns).

## S6. HEAT GENERATION OF A SINGLE DOMAIN SPHERICAL NANOPARTICLE

Figure S7 (A) includes the magnetization reversal as a function of the applied magnetic field and time. Regions marked as 1 and 3 correspond to the magnetization purely oriented along the  $z$ -axis (see (B)), whereas region 2 marks the area where the magnetization points perpendicular to the field direction. This region corresponds to the heat release, included in (C) as instantaneous heat release (gray line) and energy accumulated within the probed period. In (D), the heating and magnetization mappings are shown for the moment of maximum heat release. Contrary to the vortex-like textures discussed in the work, the heat release of single-domain particles is homogeneous. Note the difference to Fig. 4 of the main text, where the heat release is purely concentrated along the vortex core direction, and extended over tens of nanoseconds, whereas in the single-domain case, the heat is released an order of magnitude faster ( $t \sim 5$  ns).

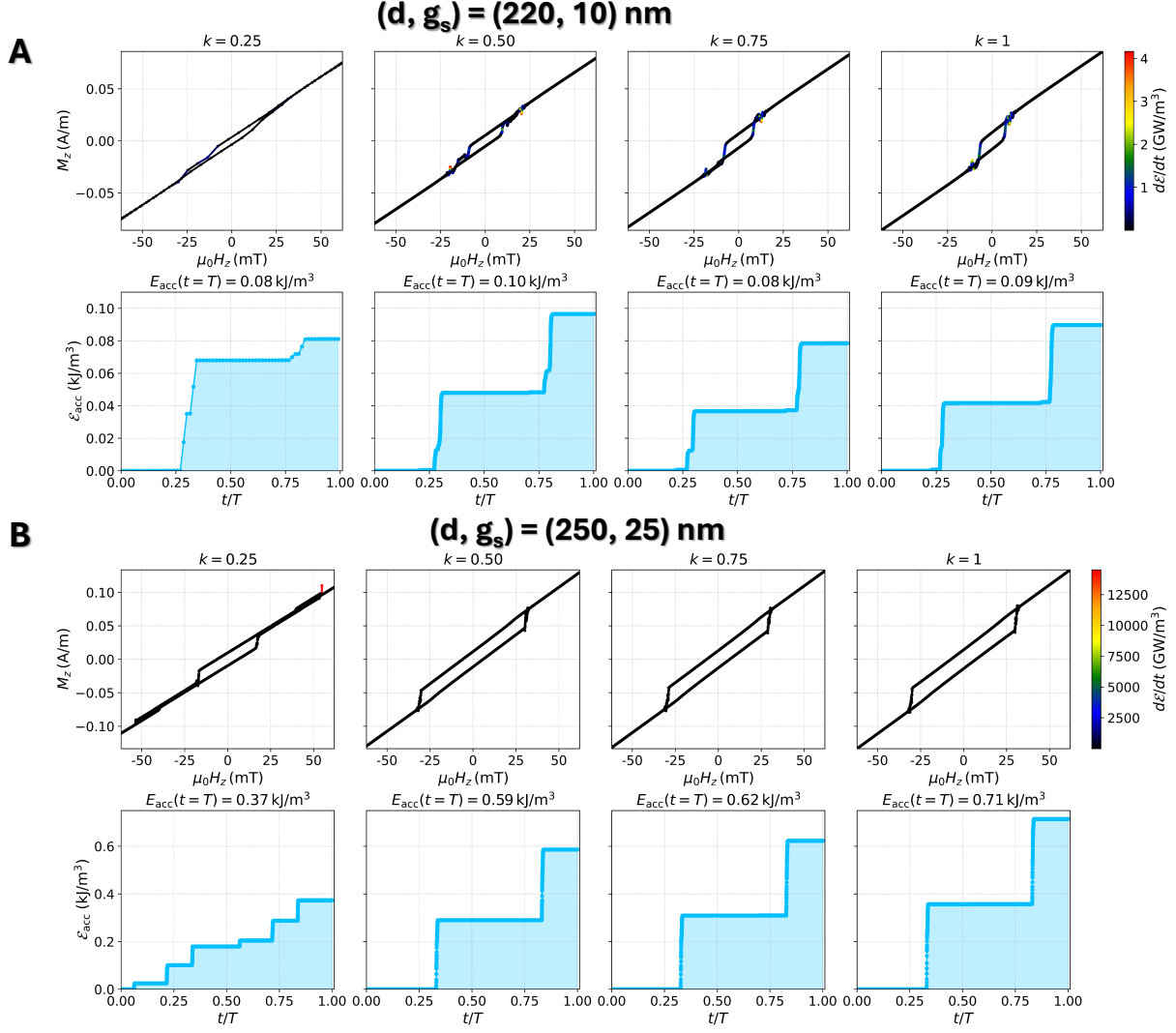


FIG. S5. Magnetization as a function of applied field and corresponding released energy  $\mathcal{E}(t)$  over one AC-field period  $T = 1/300$  ms for NFs with diameters  $d = 220$  nm and  $g_s = 10$  nm (**A**), and  $d = 250$  nm and  $g_s = 25$  nm (**B**). The magnetization traces are colour-coded by the instantaneous heat generation, with red highlighting the points of maximum dissipation, coinciding with the jumps observed in the magnetization consequence of the reversal, *i.e.* moments of maximized torque. The step-like increases in  $\mathcal{E}(t)$  coincide with these dissipation bursts. Inter-grain exchange is fixed to  $k \times A$ , with  $k = 1.00$ .

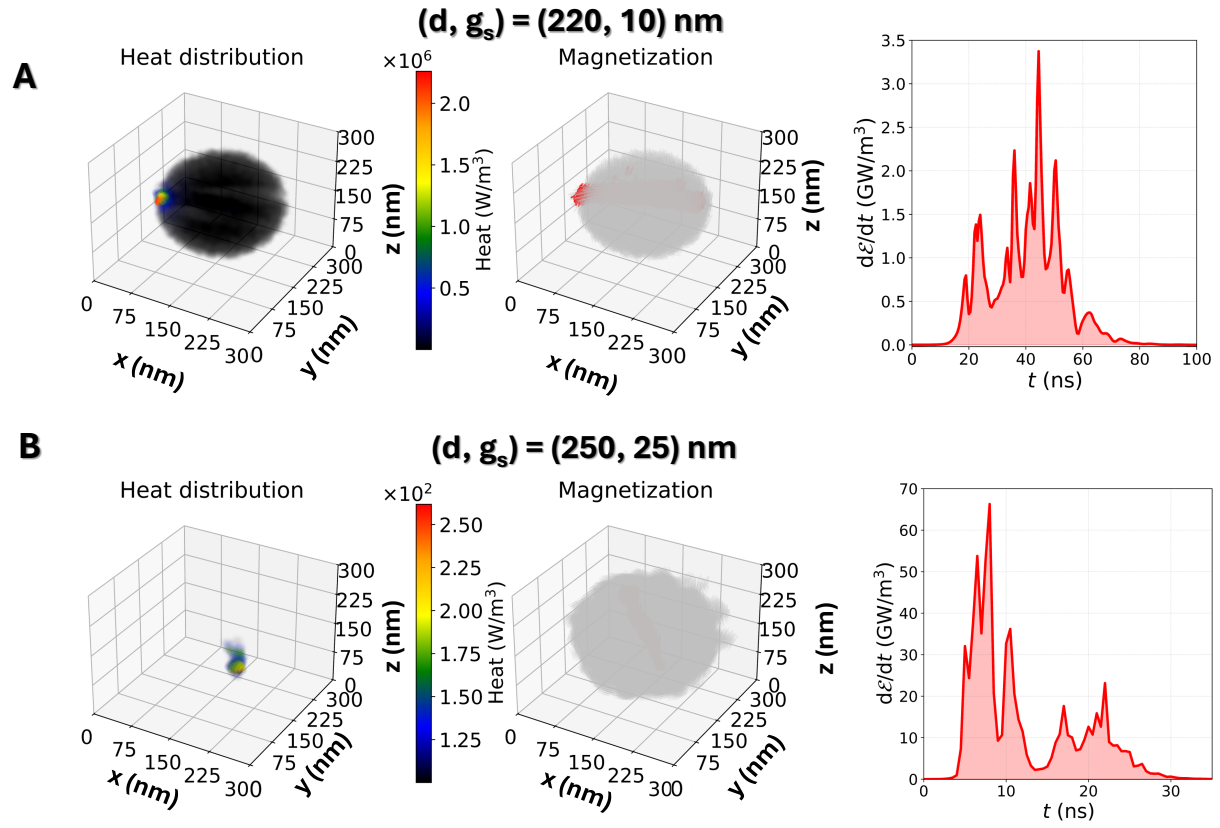


FIG. S6. 3D heat and magnetization mappings, along with the instantaneous heat release  $d\mathcal{E}/dt$  vs.  $t$ , for **(A)**  $(d, g_s) = (220, 10)$  nm, and **(B)**  $(d, g_s) = (250, 25)$  nm, respectively. Inter-grain exchange is fixed to  $k \times A$ , with  $k = 1.00$ .

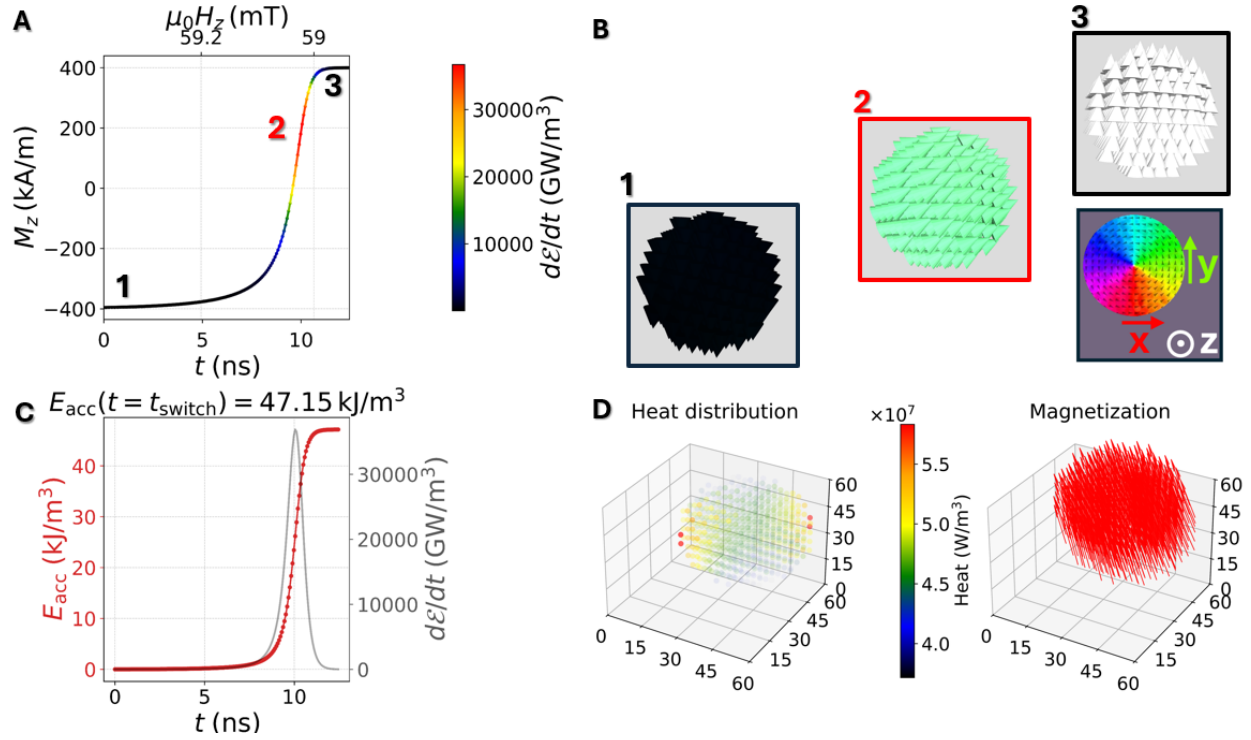


FIG. S7. Single-domain 50 nm diameter nanosphere. **(A)** Magnetization as a function of applied field (top axis) and time (bottom axis). The magnetization traces are colour-coded by the instantaneous heat generation, with red highlighting the points of maximum dissipation. **(B)** Snapshots of three representative time steps of the magnetization reversal: 1 and 3 correspond to the magnetization along  $z$ -axis, 2 to the magnetization along the  $y$  direction. We have included the colour-coded wheel on the right side. **(C)** Instantaneous heat release (grey) and energy accumulated (red) for the reversal process, which happens within 5 nanoseconds. **(D)** temperature and magnetization mappings corresponding to the moment of maximum heat release. The heat is spread along the whole nanoparticle.

- 
- [1] T. J. Collins, *Biotechniques* **43**, S25 (2007).
- [2] B. D. Cullity and S. R. Stock, *Elements of X-Ray Diffraction*, 3rd ed. (Prentice Hall / Pearson, Upper Saddle River, NJ, 2001).
- [3] R. Hergt and S. Dutz, *Journal of Magnetism and Magnetic Materials* **311**, 187 (2007).
- [4] R. Hergt, S. Dutz, and M. Zeisberger, *Nanotechnology* **21**, 015706 (2009).
- [5] E. M. Jefremovas, L. Gandarias, I. Rodrigo, L. Marcano, C. Grüttner, J. Á. García, E. Garayo, I. Orue, A. García-Prieto, A. Muela, *et al.*, *IEEE Access* **9**, 99552 (2021).
- [6] J. M. Coey, *Magnetism and magnetic materials* (Cambridge University Press, 2010).
- [7] G. Di Fratta, C. Serpico, and M. d'Aquino, *Physica B* **407**, 1368 (2012).
- [8] E. M. Jefremovas, L. Calus, and J. Leliaert, *Small Science* **6**, e202500490 (2026).
- [9] M. Coïsson, G. Barrera, F. Celegato, L. Martino, S. N. Kane, S. Raghuvanshi, F. Vinai, and P. Tiberto, *Biochimica et Biophysica Acta (BBA)-General Subjects* **1861**, 1545 (2017).
- [10] K. Simeonidis, C. Martinez-Boubeta, D. Serantes, S. Ruta, O. Chubykalo-Fesenko, R. Chantrell, J. Oró-Solé, L. Balcells, A. Kamzin, R. Nazipov, *et al.*, *ACS applied nano materials* **3**, 4465 (2020).
- [11] E. Myrovali, K. Papadopoulos, G. Charalampous, P. Kesapidou, G. Vourlias, T. Kehagias, M. Angelakeris, and U. Wiedwald, *ACS Omega* **8**, 12955 (2023).
- [12] X. Liu, Y. Zhang, Y. Wang, W. Zhu, G. Li, X. Ma, Y. Zhang, S. Chen, S. Tiwari, K. Shi, *et al.*, *Theranostics* **10**, 3793 (2020).